

Stabilization of sliding ferroelectricity through exciton condensation

Matteo D'Alessio,^{1,2} Daniele Varsano,² Elisa Molinari,^{1,2} and Massimo Rontani²

¹ University of Modena e Reggio Emilia, Department of Physics,
Informatics and Mathematics, Via Campi 213a, 41125 Modena, Italy
² CNR Nanoscience Institute, Via Campi 213a, 41125 Modena, Italy

Sliding ferroelectricity is a phenomenon that arises from the insurgence of spontaneous electronic polarization perpendicular to the layers of two-dimensional (2D) systems upon the relative sliding of the atomic layer constituents. Because of the weak van der Waals (vdW) interactions between layers, sliding and the associated symmetry breaking can occur at low energy cost in materials such as transition-metal dichalcogenides. Here we discuss theoretically the origin and quantitative understanding of the phenomenon by focusing on a prototype structure, the WTe₂ bilayer, where sliding ferroelectricity was first experimentally observed. We show that excitonic effects induce relevant energy band renormalizations in the ground state, and exciton condensation contributes significantly to stabilizing ferroelectricity upon sliding beyond previous predictions. Enhanced excitonic effects in 2D and vdW sliding are general phenomena that point to sliding ferroelectricity as relevant for a broad class of important materials, where the intrinsic electric dipole can couple with other quantum phenomena and, in turn, an external electric field can control the quantum phases through ferroelectricity in unexplored ways.

Introduction

Since the discovery of ferroelectricity in the layered semimetal WTe₂ [1] and the proposed sliding mechanism [2], the interest in sliding ferroelectricity has boomed and the pool of 2D candidate materials has significantly grown [3–21]. This interest is motivated by both fundamental scientific questions and potential technological applications. Interlayer sliding is an intrinsic mechanism, and it can drive ferroelectricity in an important class of materials, where it can couple to other quantum phenomena of great scientific interest [22–28]. Reciprocally, through ferroelectricity an external vertical electric field could control quantum phases of these 2D systems in unexplored ways, including e.g. topological, ferromagnetic or optical transitions [29–39]. From the technological point of view, the search for efficient 2D ferroelectrics is considerably more promising in vdW materials than in conventional semiconductors: Owing to the weak vdW interaction between atomic planes, combined with strong in-plane bonding, sliding parallel to the 2D planes takes place with limited energy cost and without significant vertical distortions [40, 41]. This could, for example, enable high-speed data writing and memory devices, as well as the integration of multiple functions in future nanoelectronics and spintronics [42–46].

A full quantitative understanding of sliding ferroelectricity is however still lacking. To illustrate this point, let

us focus on the paradigmatic case of the WTe₂ bilayer, the first system where it was observed experimentally and attributed to interlayer charge redistribution, in spite of its metallic character [1]. Bilayer WTe₂ is attractive because it was experimentally shown that its polarization does not vanish up to room temperature; moreover, it retains its switching capability at 300 K even when embedded in 2D devices [1].

The open question has to do with the very mechanism inducing ferroelectricity in this system. There is consensus on the fact that an in-plane sliding along a specific direction (*y* for bilayer WTe₂ as shown in Fig. 1a) changes the charge distribution between the layers and thus the electric polarization, as initially proposed theoretically [3, 47]: the sign of the polarization is reversed when the shift takes place in the opposite direction. However, while descriptions of this process based on density functional theory (DFT) lead to an interlayer charge transfer compatible with the measured polarization [2, 48], they are unable to account for the high Curie temperature observed in experiments: an issue of relevance in view of room-temperature operation, as also discussed in Refs. 49–51.

Here we move from the recent evidence of important excitonic effects in mono- and bi-layer WTe₂, leading to a ground-state excitonic insulator (EI) phase [52, 53], and analyze the role that electron-hole (e-h) interaction can play in the ferroelectric properties of bilayer WTe₂. These effects were not taken into account in previous theoretical studies, although a suggestion was already present in Ref. 1 based on the observation of identical electron and hole densities in the ferroelectric phase (as well as in Ref. 26 for MoTe₂, but in the superconducting phase). After analyzing the uncorrelated ground state from first principles, we develop a model to account for e-h interactions forming tightly-bound excitons, in order to calculate how they modify the electronic structure of the system and in turn estimate how this affects its energy.

We find that the bilayer can undergo a transition to a ground-state excitonic phase: The repulsion of the renormalized conduction and valence bands accounts for the energy cost of exciton ionization and makes the bilayer either semimetal or insulating. In all events, the energy of the system is lowered. This process induces a relevant change in the energy barrier for the sliding process, thus showing that excitonic effects can contribute significantly to the energetics of the ferroelectric switching.

Our work indicates that electronic correlations and a theoretical description beyond DFT can be relevant for

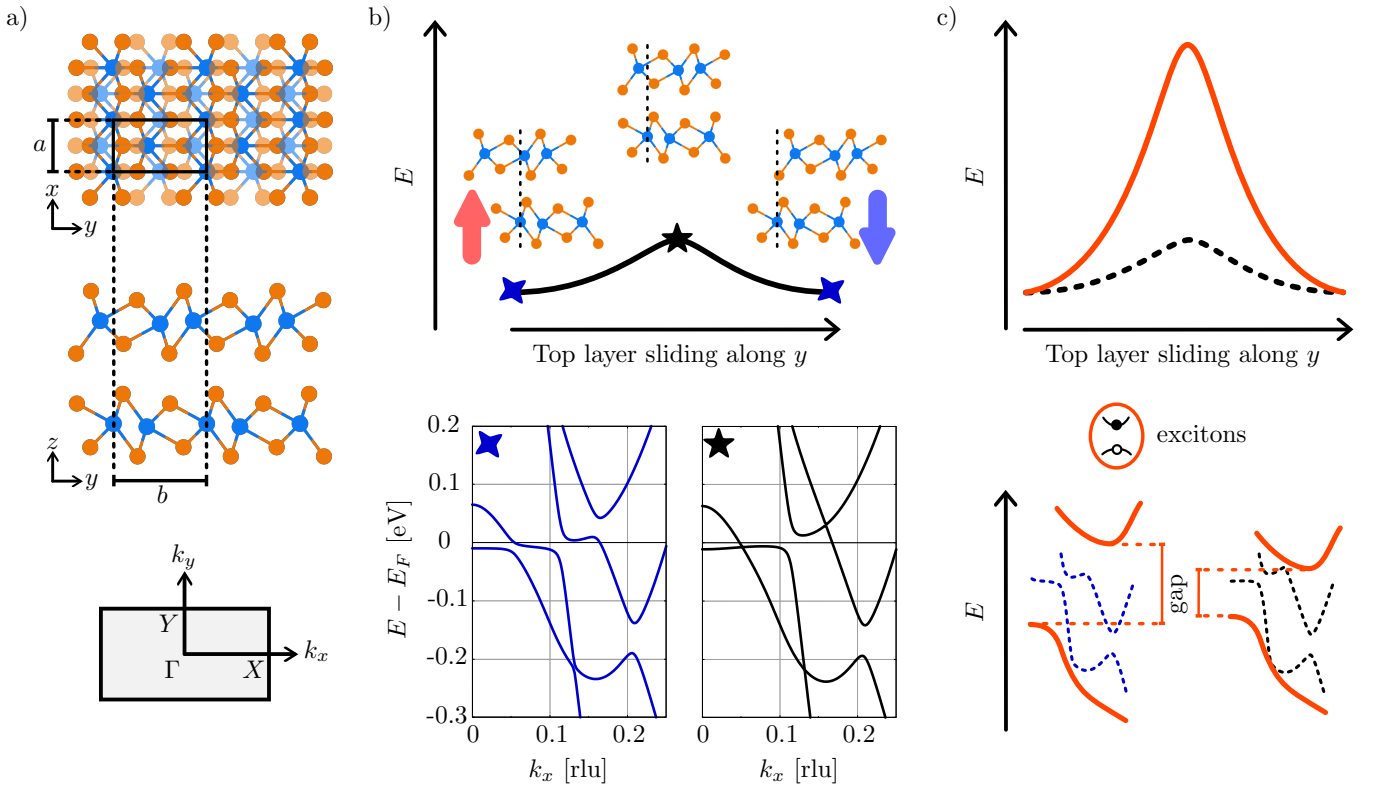


FIG. 1. **The potential barrier for the sliding process.** a) Top view, side view and Brillouin zone of bilayer WTe₂. In the top view the top layer is shaded for better clarity and the black rectangle marks the unit cell with the corresponding lattice parameters a and b . Blue atoms represent W, orange ones Te. b) Top: sketch of the energy barrier of the sliding process. The two equivalent ground states have opposite out-of-plane polarization (up/down arrows). The configuration corresponding to the energy maximum is the GMS structure. The top layer displacement from the GMS structure to the ground state structure is largely magnified in this sketch. Bottom: DFT-PBE bands corresponding to the ground state structure (left) and to the GMS structure (right). The bands are plotted along the Γ -X path and the zero of the energy axis is the Fermi energy, E_F . c) Effects of the formation of the excitonic insulator phase (red curves). The sketch shows that tightly bound excitons can modify the band structure (bottom), and possibly open a gap, hence lowering the energy of the system and thus changing the energy barrier for the sliding process (top). The red solid bands represent qualitatively how the DFT bands change after including excitonic effects; the dashed bands, shown as reference, reproduce the DFT-PBE bands of panel b) around E_F for the displaced and GMS structures (left and right, respectively).

2D vdW systems, even for phenomena such as sliding ferroelectricity where they are typically neglected. Importantly, it indicates that such contribution can stabilize sliding ferroelectricity beyond previous predictions, which increases the conceptual and technological interest of this phenomenon in the broader class of 2D vdW materials. Figure 1 summarizes the main ideas that we will discuss in the following paragraphs. The structure of a WTe₂ bilayer is shown in Fig. 1a, in particular the non polar configuration that we label with a black star in the rest of Fig. 1. We refer to this configuration as *glide-mirror symmetric* (GMS) structure. The next two columns of the figure respectively schematize the picture emerging from single-particle DFT calculations (Fig. 1b) and from a description that includes excitonic effects (Fig. 1c).

Results

Starting from the DFT picture

Let us first consider the picture obtained by means of a first-principles description at the DFT level. When one of the WTe₂ layers of the GMS structure, say the top one, is shifted horizontally with respect to the bottom layer, the energy of the system is lowered. The new configuration, marked by a blue diamond in Fig. 1b, is characterized by a finite polarization perpendicular to the layers. Because of the symmetry of the crystal structure, in bilayer WTe₂ this sliding mechanism connects two energetically equivalent ground states with opposite out-of-plane polarization. We estimated the energy barrier for this process, sketched in Fig. 1b, by means of a DFT nudged elastic band (NEB) calculation obtaining a value of 0.4 meV, compatible with previous results [2, 48].

Figure 1b also shows the band structure for both unpolarized and ground-state polarized configurations, as obtained by DFT calculations within the generalized gradient approximation for the exchange-correlation func-

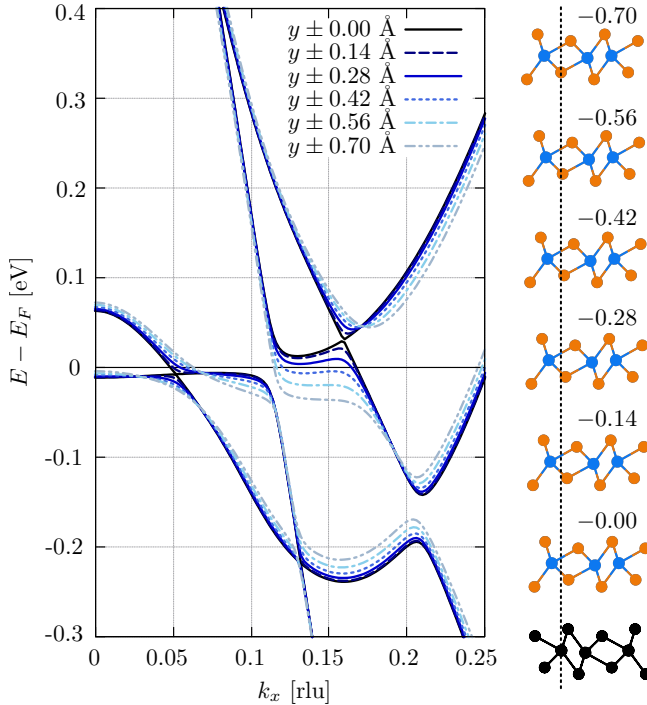


FIG. 2. **Effect of layer sliding on band structure.** DFT-PBE bands for different displacements of the top layer along the sliding direction. The plot shows the cut along ΓX (thus $k_y = 0$); k_x is in units of the corresponding reciprocal lattice vector (rlu). The bottom layer (dyed in black) is fixed and 0.00 displacement of the top layer corresponds to the GMS structure. Images on the right show the displacements of the top layer (coloured) in real scale, with the dashed line indicating the fixed position of the bottom layer; negative values of the displacements are indicated in Å, as in the key; positive displacements – not shown – are analogous and give the same bands.

tional. Note that spin-orbit coupling (SOC) is not included in these calculations as it leads to minor corrections for the natural stacking of the layers considered here, at difference with geometries that preserve the inversion symmetry [54]. A systematic display of band structure results for increasing relative displacement of the layers is given in Fig. 2. Among these values, the displacement $\bar{d} = 0.28$ Å gives the lowest total energy in the DFT calculation. The corresponding bands are represented by a solid blue line, as in Fig. 1b. Note that, at this level of description, the system is semimetallic. We expect the gap opening effect of DFT hybrid functionals [55, 56] essentially not to alter the predicted energy barrier.

The comparison of DFT-level calculations with experiments is intriguing. On one side, the charge transfer between the layers, as computed from the ground state charge density, gives an areal polarization density of 1.5×10^4 e/cm, in agreement with the experimental measurements [1] and previous theoretical results [2, 48]. On the other side, the estimated energy barrier does not

clarify how this material can retain its ferroelectric properties at high temperatures. In addition, the metallic character resulting from the calculated band structure is at odds with the measured transport gap of a few meV [52].

Beyond DFT: including excitonic interactions

In the following we analyze how this picture is modified by the effects of e-h interaction, to assess the possible contribution of an excitonic phase to ferroelectricity. To make the problem tractable, we introduce some approximations. We consider spinless excitons, as spin effects are unlikely to affect ferroelectricity. Furthermore, we take that all condensing excitons have zero momentum, $\mathbf{q}_x = 0$ (direct transitions). Otherwise, the excitons would sustain a charge density wave, with period related to the momentum \mathbf{q}_x . Since for all possible choices of \mathbf{q}_x the charge modulation would encompass at least two lattice units, the net coupling of the density wave with the macroscopic electronic dipole would likely average out.

A full first-principles treatment is beyond our scope, as predictive accuracy requires computational tasks that are demanding for a semimetal, such as the calculation of the GW correction to band structure including dynamical screening effects, as well as the evaluation of the intraband contribution to electronic polarizability [57–62]. Therefore, we rely on the envelope function approximation, which allows us to both solve the exciton problem and compute the renormalized band structure of the excitonic insulator, building on DFT results. Importantly, we model the e-h attraction through the Rytova-Keldysh potential [63–65], which parametrizes the interaction strength through a single parameter, the 2D polarizability of the bilayer, α_{2D} , as defined in Eq. (3).

We start by writing the (Bethe-Salpeter) equation of motion of excitons based on the DFT-PBE band structure of Fig. 2. Whereas our framework works for an arbitrary number of bands, here we limit their number to two for the sake of simplicity (results from a four-band model are shown for comparison in Supplementary Figure 1). We use the highest valence ($i = 1$) and lowest conduction ($i = 2$) bands of Fig. 2, which are separated by gaps at $k_x \approx 0.12$ rlu and $k_x \approx 0.21$ rlu, respectively, as the eigenvalues $\varepsilon_i(\mathbf{k})$ of the noninteracting Hamiltonian $H_0(\mathbf{k})$, a 2×2 diagonal matrix in \mathbf{k} space. The two bands, which are partially filled in the semimetal ground state predicted by DFT, become either occupied or empty in the excitonic insulator phase. The eigenvalue problem for the excitons is

$$\sum_{\mathbf{k}'} H_{\mathbf{k}}^{\mathbf{k}'} \Psi_{\mathbf{x}}^{\mathbf{k}'} = E_{\mathbf{x}} \Psi_{\mathbf{x}}^{\mathbf{k}}, \quad (1)$$

with the exciton Hamiltonian matrix element, $H_{\mathbf{k}}^{\mathbf{k}'}$, being

$$H_{\mathbf{k}}^{\mathbf{k}'} = [\varepsilon_2(\mathbf{k}) - \varepsilon_1(\mathbf{k})] \delta_{\mathbf{k}, \mathbf{k}'} - W(\mathbf{k} - \mathbf{k}'). \quad (2)$$

Here $\Psi_{\mathbf{x}}^{\mathbf{k}}$ is the exciton wave function, i.e., the probability amplitude for exciting an electron from valence to conduction band conserving its momentum \mathbf{k} , $E_{\mathbf{x}}$ is the exciton energy, and $W(\mathbf{q})$ is the e-h attraction that transfers

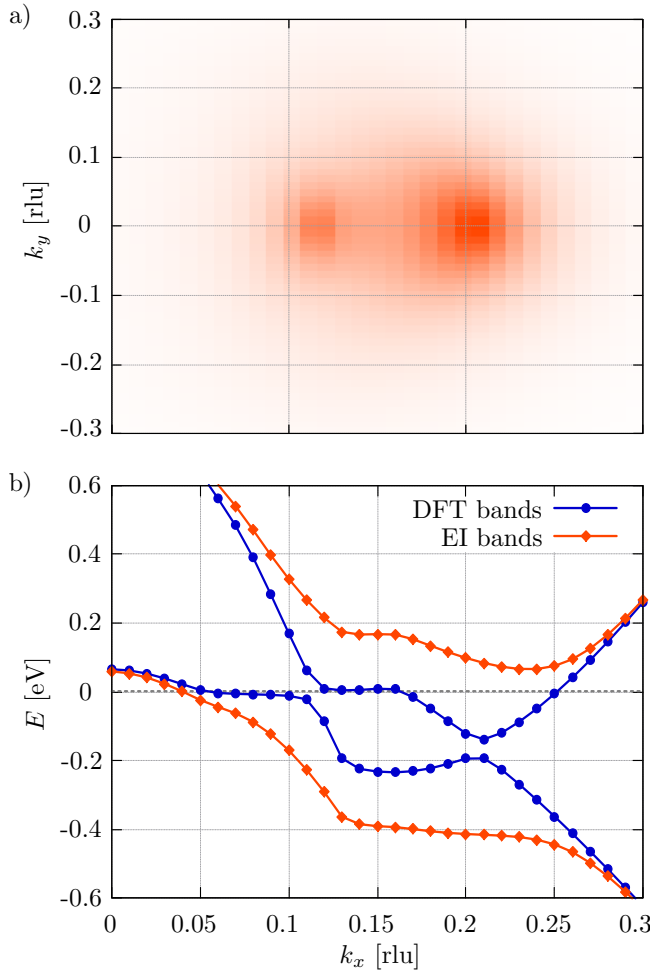


FIG. 3. **Excitons and excitonic insulator.** a) Exciton wave function in \mathbf{k} space. The contour plot represents the probability amplitude Ψ_x^k of exciting an e-h pair by transferring an electron from the valence to the conduction band state at fixed momentum (k_x, k_y) . The range of the color scale is $[0, 0.11]$. b) Condensation of excitons leads to the reconstruction of the bands (EI) with the opening of a gap. The plot shows the cut for $k_y = 0$. For both panels the layer displacement is \bar{d} and $\alpha_{2D} = 4.3$ Å.

momentum \mathbf{q} between e-h pairs. In view of the postulated exciton condensation, we assume bands 1 and 2 to be respectively filled and empty, hence $\varepsilon_2(\mathbf{k}) - \varepsilon_1(\mathbf{k})$ is always positive. The explicit form of W [63–65] is

$$W(q) = \frac{e^2}{2\varepsilon_0 A} \frac{1}{q(1 + 2\pi \alpha_{2D} q)}, \quad (3)$$

where A is the unit cell area and ε_0 the vacuum permittivity.

Figure 3a plots the contour map of Ψ_x^k obtained for the equilibrium layer displacement \bar{d} and e-h attraction strength sufficient to open a gap in the excitonic phase, $\alpha_{2D} = 4.3$ (this choice gives a tiny gap of 3 meV in the GMS structure). The resulting binding energy is 256 meV, smaller than the one we obtained for the monolayer,

~ 300 meV [52]. This is reasonable, as the electronic screening should be more effective in the bi- than in the mono-layer. The maximum amplitude of Ψ_x^k is reached at the two locations in the Brillouin zone region shown in Fig. 3a that correspond to the two energy gaps along the Γ X cut, where the excitation energy of free e-h pairs is lower. Note that Ψ_x^k may be regarded as a proxy of the macroscopic wave function of the exciton condensate [66] that we evaluate below, the discrepancies arising from Pauli blockade effects when condensing excitons fill in the phase space. Therefore, we anticipate that the Brillouin zone region where the band renormalization due to the condensate is stronger approximately mirrors the map of Ψ_x^k (Fig. 3b).

Contribution of exciton condensation to the ferroelectric transition

We next investigate whether the formation of bound e-h pairs, the excitons, can be energetically favorable in the initial semimetal state, such that the system will undergo a transition to the ‘excitonic’ insulator (EI) [67–69] or semimetal [70] phase. In EIs, excitons form spontaneously, i.e., in the absence of any photoexcitation, condense, and collectively sustain the reconstruction of the bands and the onset of a gap. A condition for energy gain in the EI formation is a large exciton binding energy, which in some 2D systems can be achieved thanks to the reduced screening of the e-h Coulomb interaction, as we have demonstrated for WTe₂ monolayer [52].

To explore the possibility of this kind of transition in bilayer WTe₂ driven by the formation of direct excitons, we extend the model of Ref. 68 to our case, which in principle includes several bands. The excitonic insulator state is written as

$$|\Psi_{EI}\rangle = \prod_{i\mathbf{k}} \hat{a}_{i\mathbf{k}}^\dagger |\text{vac}\rangle, \quad (4)$$

where the EI valence band annihilation operators $\hat{a}_{i\mathbf{k}}$ can be expressed as

$$\hat{a}_{i\mathbf{k}} = \sum_j a_{ij\mathbf{k}} \hat{a}_{j\mathbf{k}} \quad (5)$$

and $|\text{vac}\rangle$ is the vacuum state with no electrons. In this last expression \hat{a} is either a conduction or valence band Bloch state of the pristine semimetal and the coefficients a_{ij} form a unitary matrix, to be determined self-consistently for each \mathbf{k} point. The reconstructed bands $E_i(\mathbf{k})$ are then obtained from the diagonalization of

$$\begin{pmatrix} \varepsilon_1(\mathbf{k}) & \Delta(\mathbf{k}) \\ \Delta(\mathbf{k}) & \varepsilon_2(\mathbf{k}) \end{pmatrix}, \quad (6)$$

where $\Delta(\mathbf{k})$ is the (single) gap function for the special case of two bands. Its multiband form is

$$\Delta_{ij}(\mathbf{k}) = \sum_{l, l', \mathbf{k}'} W(\mathbf{k} - \mathbf{k}') [a_{\mathbf{k}'}^{-1}]_{jl} [a_{\mathbf{k}'}^{-1}]_{il'} \langle \hat{a}_{l\mathbf{k}'}^\dagger \hat{a}_{l'\mathbf{k}'} \rangle_{\Psi_{EI}}. \quad (7)$$

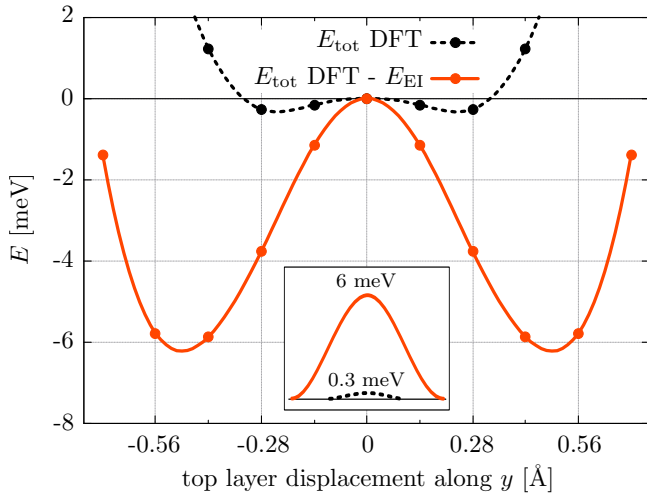


FIG. 4. **Excitonic renormalization of the sliding energy barrier.** Energy versus sliding displacement, with (solid red) and without (dashed black) e-h interaction effects. The dashed black curve is the DFT total energy; the solid red curve is obtained by subtracting the corresponding E_{EI} value. For both curves the energy zero is set at $d = 0$ displacement (GMS configuration). The interpolation lines are a guide to the eye. The inset shows, in scale, the variation of the energy barrier, which increases from 0.3 to 6 meV.

We will report extensively on the multiband analysis elsewhere, but see Supplementary Figure 1 for an example with four bands. Since the Δ 's depend on the eigenvalues $E_i(\mathbf{k})$ of the matrix above through the expectation values

$$\langle \hat{\alpha}_{l\mathbf{k}'}^\dagger \hat{\alpha}_{l'\mathbf{k}'} \rangle_{\Psi_{\text{EI}}} = \delta_{l,l'} f(E_l(\mathbf{k})) \quad (8)$$

as well as its eigenvectors $a_{\mathbf{k}}$, the problem has to be solved self-consistently (here the Fermi-Dirac function f is 1 and 0 for valence and conduction). In the first step of the self-consistent cycle the sum over l and l' is replaced by $\Psi_x^{\mathbf{k}'}$, the (lowest energy) exciton wavefunction from the solution of Eq. (2). The final, reconstructed bands $E_i(\mathbf{k})$ come from the diagonalization of the matrices in Eq. (6) with the converged values of $\Delta(\mathbf{k})$.

We are now ready to show results for the EI phase, as schematically summarized in Fig. 1c. The calculated EI reconstructed bands with the indirect narrow gap ≈ 7 meV, comparable to the measured one [52], are given in Fig. 3b for the equilibrium relative layer shift \bar{d} , compared to the starting DFT bands.

To estimate the energy gain in the EI phase for all the top layer displacements, we start from the plot of the DFT total energy E_{tot} as a function of the sliding along y (Fig. 4, black dashed line). Without considering the excitonic effects, the energy difference between displacements 0 and \bar{d} is ≈ 0.3 meV, which is comparable with the NEB barrier.

We now evaluate the total energy gain due to exciton

condensation, E_{EI} , as

$$E_{\text{EI}} = \frac{2}{N_{\mathbf{k}}} \sum_{\mathbf{k}} [\varepsilon_{1,\text{occ}}(\mathbf{k}) + \varepsilon_{2,\text{occ}}(\mathbf{k}) - E_1(\mathbf{k})] + \frac{E_{\text{gap}}}{2}. \quad (9)$$

Here $\varepsilon_{i,\text{occ}}(\mathbf{k})$ are the occupied (i.e. $\varepsilon \leq E_F$) DFT energy bands, $E_1(\mathbf{k})$ is the reconstructed valence band energy for the EI phase, lowered by $-E_{\text{gap}}/2$ (at zero temperature the chemical potential is in the middle of the gap), $N_{\mathbf{k}}$ is the total number of k-points sampling the Brillouin zone, and the factor 2 accounts for spin degeneracy. Note that Eq. (9) holds only for the insulating phase. For the semimetallic excitonic phase, $E_{\text{gap}} = 0$, and $E_1(\mathbf{k})$ in Eq. (9) must be replaced with $E_{1,\text{occ}}(\mathbf{k}) + E_{2,\text{occ}}(\mathbf{k})$, where E_F has to be determined self-consistently, for each step of the iterative cycle. It is then immediate to check that $E_{\text{EI}} = 0$ in the absence of excitonic effects.

Importantly, the variations in the starting DFT bands and their anticrossings (Fig. 2) impact the final $E_i(\mathbf{k})$ bands and E_{gap} in a significant way. It follows that the energy gain E_{EI} is highly sensitive to the sliding displacement value d along y , as clear from Fig. 4 (solid red curve). Namely, the energy difference between the ferroelectric structure ($d = \bar{d}$ displacement) and the GMS structure ($d = 0$) with no dipole is modified from 0.3 meV to ≈ 4 meV. For a displacement of 0.4 Å this value increases up to around 6 meV, or 70 K in terms of temperature.

Overall, the energy barrier for the sliding process is heavily renormalized by condensation, due to the sensitivity of exciton binding to the modifications of the band structure. This is in contrast with the total energy gain, E_{BCS} , in the BCS theory for superconductors, which is formally analogous to our treatment of the semimetallic phase. It is a textbook result [71] that $E_{\text{BCS}} \sim \Delta^2/E_F \sim 10^{-2}$ K is orders of magnitude smaller for conventional superconductors, since the Cooper pair binding energy, Δ , is a tiny fraction of E_F .

Discussion and conclusions

Our theory shows that a gap opening in bilayer WTe₂ is induced by the condensation of direct excitons. Whereas the absolute value of the indirect gap depends on the screening parameter α_{2D} , the gap size variation (and in turn E_{EI}) with the layer shift coordinate d does not, as illustrated from Supplementary Figure 2. Therefore, our estimate of the ‘excitonic’ barrier height should be robust against the uncertainty associated with the simplified approach.

In conclusion, we have pointed out that e-h interaction effects can play an important role in sliding ferroelectricity that is not captured by a first-principles description at the DFT level. For the WTe₂ prototype bilayer we show that, as long as exciton coherence survives, relevant modifications result in the energetics of the system that contribute to stabilize ferroelectricity upon sliding.

We expect that relevant excitonic contributions will be present in general throughout 2D systems, where e-h Coulomb interactions are greatly enhanced by the re-

duced screening. Combined with the easy relative sliding typical of van der Waals layers, these results indicate that 2D sliding ferroelectricity may be even more widespread and robust than previously expected.

Methods

DFT and NEB calculations are performed using the Quantum ESPRESSO package [72]. We adopt the Perdew-Burke-Ernzerhof (PBE) approximation for the exchange-correlation functional [73] and norm-conserving pseudopotentials [74]. Unless otherwise specified, the cutoff value for plane wave expansion of wave functions is 100 Ry and the Brillouin zone is sampled by a 22×12 Monkhorst-Pack grid of k-points [75]. Van der Waals interactions are taken into account through the Grimme-D3 method [76] with Becke-Johnson damping [77]. Spurious interactions between periodic replicas in the out-of-plane direction are avoided by setting the cell dimension along z to 40 Å. NEB calculations employ the climbing image scheme to determine the transition path [78], with a 0.05 eV/Å threshold on the forces orthogonal to the path. The optimized lattice parameters and atomic positions are obtained by means of a structure relaxation with a threshold of 1 meV/Å on atomic forces and a cut-off value of 200 Ry for the plane wave expansion. The resulting values are 3.473 Å and 6.276 Å for the x and

y cell parameters respectively. The model BSE and EI gap equation are implemented in a custom code available upon request. The k-points in the calculations discussed here sample the region of the BZ corresponding to $k_x = [0, 0.3]$ and $k_y = [-0.3, 0.3]$ [rlu] with a 30×60 mesh. In the self-consistent gap equation we check convergence on the values of $\Delta(\mathbf{k})$: the cycle stops at the n -th step if $|\Delta^{[n-1]}(\mathbf{k}) - \Delta^{[n]}(\mathbf{k})| < \varepsilon_{\text{thr.}}$, and we set $\varepsilon_{\text{thr.}} = 0.5$ meV.

Acknowledgments

We are grateful to Giacomo Sesti and Claudia Cardoso for many useful discussions. Access to high performance computing resources was provided by EuroHPC Joint Undertaking (JU) through the project EHPC-EXT-2022E01-022 and ISCRA, that granted access to the LEONARDO supercomputer, owned by the EuroHPC JU, hosted by CINECA (Italy). This work was supported in part by: the MaX – MAterials design at the eXascale – European Centre of Excellence, co-funded by the EuroHPC JU and Ministero delle Imprese e del Made in Italy (grant agreement No. 101093374); ICSC – Centro Nazionale di Ricerca in High Performance Computing, Big Data and Quantum Computing – funded by the European Union through the Italian Ministry of University and Research under PNRR M4C2I1.4 (grant CN00000013).

[1] Z. Fei, W. Zhao, T. A. Palomaki, B. Sun, M. K. Miller, Z. Zhao, J. Yan, X. Xu, and D. H. Cobden, Ferroelectric switching of a two-dimensional metal, *Nature* **560**, 336 (2018).

[2] Q. Yang, M. Wu, and J. Li, Origin of Two-Dimensional Vertical Ferroelectricity in WTe₂ Bilayer and Multilayer, *The Journal of Physical Chemistry Letters* **9**, 7160 (2018).

[3] M. Wu and J. Li, Sliding ferroelectricity in 2D van der Waals materials: Related physics and future opportunities, *Proceedings of the National Academy of Sciences* **118**, e2115703118 (2021).

[4] C. Wang, L. You, D. Cobden, and J. Wang, Towards two-dimensional van der Waals ferroelectrics, *Nature Materials* **22**, 542 (2023).

[5] S. C. de la Barrera, Q. Cao, Y. Gao, Y. Gao, V. S. Bheemarasetty, J. Yan, D. G. Mandrus, W. Zhu, D. Xiao, and B. M. Hunt, Direct measurement of ferroelectric polarization in a tunable semimetal, *Nature Communications* **12**, 5298 (2021).

[6] M. Vizner Stern, Y. Waschitz, W. Cao, I. Nevo, K. Watanabe, T. Taniguchi, E. Sela, M. Urbakh, O. Hod, and M. Ben Shalom, Interfacial ferroelectricity by van der Waals sliding, *Science* **372**, 1462 (2021).

[7] X. Ma, C. Liu, W. Ren, and S. A. Nikolaev, Tunable vertical ferroelectricity and domain walls by interlayer sliding in β -ZrI₂, *npj Computational Materials* **7**, 177 (2021).

[8] T. Zhang, Y. Liang, X. Xu, B. Huang, Y. Dai, and Y. Ma, Ferroelastic-ferroelectric multiferroics in a bilayer lattice, *Phys. Rev. B* **103**, 165420 (2021).

[9] R. Niu, Z. Li, X. Han, Z. Qu, D. Ding, Z. Wang, Q. Liu, T. Liu, C. Han, K. Watanabe, T. Taniguchi, M. Wu, Q. Ren, X. Wang, J. Hong, J. Mao, Z. Han, K. Liu, Z. Gan, and J. Lu, Giant ferroelectric polarization in a bilayer graphene heterostructure, *Nature Communications* **13**, 6241 (2022).

[10] P. Meng, Y. Wu, R. Bian, E. Pan, B. Dong, X. Zhao, J. Chen, L. Wu, Y. Sun, Q. Fu, Q. Liu, D. Shi, Q. Zhang, Y.-W. Zhang, Z. Liu, and F. Liu, Sliding induced multiple polarization states in two-dimensional ferroelectrics, *Nature Communications* **13**, 7696 (2022).

[11] L.-P. Miao, N. Ding, N. Wang, C. Shi, H.-Y. Ye, L. Li, Y.-F. Yao, S. Dong, and Y. Zhang, Direct observation of geometric and sliding ferroelectricity in an amphidynamic crystal, *Nature Materials* **21**, 1158 (2022).

[12] X. Wang, K. Yasuda, Y. Zhang, S. Liu, K. Watanabe, T. Taniguchi, J. Hone, L. Fu, and P. Jarillo-Herrero, Interfacial ferroelectricity in rhombohedral-stacked bilayer transition metal dichalcogenides, *Nature Nanotechnology* **17**, 367 (2022).

[13] F. Sui, M. Jin, Y. Zhang, R. Qi, Y.-N. Wu, R. Huang, F. Yue, and J. Chu, Sliding ferroelectricity in van der Waals layered γ -InSe semiconductor, *Nature Communications* **14**, 36 (2023).

[14] Y. Wan, T. Hu, X. Mao, J. Fu, K. Yuan, Y. Song, X. Gan, X. Xu, M. Xue, X. Cheng, C. Huang, J. Yang, L. Dai, H. Zeng, and E. Kan, Room-Temperature Ferroelectricity in 1T'-ReS₂ Multilayers, *Phys. Rev. Lett.* **128**, 067601 (2022).

[15] K. Liu, X. Ma, S. Xu, Y. Li, and M. Zhao, Tunable sliding ferroelectricity and magnetoelectric coupling in two-dimensional multiferroic MnSe materials, *npj Computational Materials* **9**, 16 (2023).

[16] Z. Wang, Z. Gui, and L. Huang, Sliding ferroelectricity in bilayer honeycomb structures: A first-principles study, *Physical Review B* **107**, 035426 (2023).

[17] L. Yang and M. Wu, Across-Layer Sliding Ferroelectricity in 2D Heterolayers, *Advanced Functional Materials* **33**, 2301105 (2023).

[18] N. Ding, H. Ye, and S. Dong, Quasi-one-dimensional sliding ferroelectricity in NbI₄, *Phys. Rev. B* **110**, 024115 (2024).

[19] S. Pakdel, A. Rasmussen, A. Taghizadeh, M. Kruse, T. Olsen, and K. S. Thygesen, High-throughput computational stacking reveals emergent properties in natural van der Waals bilayers, *Nature Communications* **15**, 932 (2024).

[20] L. Zhang, J. Ding, H. Xiang, N. Liu, W. Zhou, L. Wu, N. Xin, K. Watanabe, T. Taniguchi, and S. Xu, Electronic ferroelectricity in monolayer graphene Moiré superlattices, *Nature Communications* **15**, 10905 (2024).

[21] Y. Wei, Z. Hu, X. Ma, H. Wang, F. Gao, X. Ma, Y. Wang, and W. Ren, In-plane sliding ferroelectricity and piezoelectricity in bilayer and trilayer g -C₃N₄, *Phys. Rev. B* **110**, 174103 (2024).

[22] J. Park, I. W. Yeo, G. Han, C. S. Hwang, and J.-H. Choi, Ferroelectric switching in bilayer 3R MoS₂ via interlayer shear mode driven by nonlinear phononics, *Scientific Reports* **9**, 14919 (2019).

[23] N. Ding, J. Chen, C. Gui, H. You, X. Yao, and S. Dong, Phase competition and negative piezoelectricity in interlayer-sliding ferroelectric ZrI₂, *Phys. Rev. Mater.* **5**, 084405 (2021).

[24] Y. Liang, N. Mao, Y. Dai, L. Kou, B. Huang, and Y. Ma, Intertwined ferroelectricity and topological state in two-dimensional multilayer, *npj Computational Materials* **7**, 172 (2021).

[25] R.-C. Xiao, Y. Gao, H. Jiang, W. Gan, C. Zhang, and H. Li, Non-synchronous bulk photovoltaic effect in two-dimensional interlayer-sliding ferroelectrics, *npj Computational Materials* **8**, 138 (2022).

[26] A. Jindal, A. Saha, Z. Li, T. Taniguchi, K. Watanabe, J. C. Hone, T. Birol, R. M. Fernandes, C. R. Dean, A. N. Pasupathy, and D. A. Rhodes, Coupled ferroelectricity and superconductivity in bilayer Td-MoTe₂, *Nature* **613**, 48 (2023).

[27] J. Shi, W. You, X. Li, F. Y. Gao, X. Peng, S. Zhang, J. Li, Y. Zhang, L. Fu, P. J. Taylor, K. A. Nelson, and E. Baldini, Revealing a distortive polar order buried in the fermi sea, *Science Advances* **10**, eadn0929 (2024).

[28] X. Zhang, P. Zhao, and F. Liu, Ferroelectric topological superconductor: α -In₂Se₃, *Phys. Rev. B* **109**, 125130 (2024).

[29] J. Xiao, Y. Wang, H. Wang, C. Pemmaraju, S. Wang, P. Muscher, E. J. Sie, C. M. Nyby, T. P. Devoreaux, X. Qian, *et al.*, Berry curvature memory through electrically driven stacking transitions, *Nature Physics* **16**, 1028 (2020).

[30] X. Liu, A. P. Pyatakov, and W. Ren, Magnetoelectric Coupling in Multiferroic Bilayer VS₂, *Phys. Rev. Lett.* **125**, 247601 (2020).

[31] J. Zhou, Photo-magnetization in two-dimensional sliding ferroelectrics, *npj 2D Materials and Applications* **6**, 1 (2022).

[32] J. Chen, W. Qin, P. Cui, and Z. Zhang, Enhanced stability and superconductivity of IrTe₂/In₂Se₃ heterobilayers with ferroelectrically switchable band topology, *Phys. Rev. B* **108**, 085408 (2023).

[33] L. Gao and L. Bellaiche, Large Photoinduced Tuning of Ferroelectricity in Sliding Ferroelectrics, *Physical Review Letters* **133**, 196801 (2024).

[34] L. Song, Y. Zhao, R. Du, H. Li, X. Li, W. Feng, J. Yang, X. Wen, L. Huang, Y. Peng, H. Sun, Y. Jiang, J. He, and J. Shi, Coexistence of Ferroelectricity and Ferromagnetism in Atomically Thin Two-Dimensional Cr₂S₃/WS₂ Vertical Heterostructures, *Nano Letters* **24**, 2408 (2024).

[35] Y. Liang, P. Zhao, F. Zheng, and T. Frauenheim, Sliding ferroelectric controllable topological phases in the Bi₂Te₃/MnBi₂Te₄ heterobilayer, *Phys. Rev. B* **111**, 035444 (2025).

[36] R. Niu, Z. Li, X. Han, Z. Qu, Q. Liu, Z. Wang, C. Han, C. Wang, Y. Wu, C. Yang, M. Lv, K. Yang, K. Watanabe, T. Taniguchi, K. Liu, J. Mao, W. Shi, R. Che, W. Zhou, J. Xue, M. Wu, B. Peng, Z. V. Han, Z. Gan, and J. Lu, Ferroelectricity with concomitant Coulomb screening in van der Waals heterostructures, *Nature Nanotechnology* **20**, 346 (2025).

[37] N.-J. Yang, J.-M. Zhang, X.-P. Li, Z. Zhang, Z.-M. Yu, Z. Huang, and Y. Yao, Sliding Ferroelectrics Induced Hybrid-Order Topological Phase Transitions, *Physical Review Letters* **134**, 256602 (2025).

[38] C. Sevik, E. Torun, M. V. Milošević, and F. Paleari, State- and Momentum-Dependent Nonlinear Stark Effect of Interlayer Excitons in Bilayer WSe₂, *Nano Letters* **25**, 9918 (2025).

[39] Y. Zhu, M. Gu, Y. Liu, X. Chen, Y. Li, S. Du, and Q. Liu, Sliding Ferroelectric Control of Unconventional Magnetism in Stacked Bilayers, *Physical Review Letters* **135**, 056801 (2025).

[40] M. Reguzzoni, A. Fasolino, E. Molinari, and M. C. Righi, Potential energy surface for graphene on graphene: Ab initio derivation, analytical description, and microscopic interpretation, *Phys. Rev. B* **86**, 245434 (2012).

[41] G. Levita, A. Cavaleiro, E. Molinari, T. Polcar, and M. C. Righi, Sliding Properties of MoS₂ Layers: Load and Interlayer Orientation Effects, *The Journal of Physical Chemistry C* **118**, 13809 (2014).

[42] R. Bian, R. He, E. Pan, Z. Li, G. Cao, P. Meng, J. Chen, Q. Liu, Z. Zhong, W. Li, and F. Liu, Developing fatigue-resistant ferroelectrics using interlayer sliding switching, *Science* **385**, 57 (2024).

[43] X. Chen, X. Ding, G. Gou, and X. C. Zeng, Strong Sliding Ferroelectricity and Interlayer Sliding Controllable Spintronic Effect in Two-Dimensional HgI₂ Layers, *Nano Letters* **24**, 3089 (2024).

[44] K. Yasuda, E. Zalys-Geller, X. Wang, D. Bennett, S. S. Cheema, K. Watanabe, T. Taniguchi, E. Kaxiras, P. Jarillo-Herrero, and R. Ashoori, Ultrafast high-endurance memory based on sliding ferroelectrics, *Science* **385**, 53 (2024).

[45] J. Liang, Y. Xie, D. Yang, S. Guo, K. Watanabe, T. Taniguchi, J. I. Dadap, D. Jones, and Z. Ye, Nanosecond Ferroelectric Switching of Intralayer Excitons in Bilayer 3R MoS₂ through Coulomb Engineering, *Physical Review X* **15**, 021081 (2025).

[46] R. Bian, G. Cao, E. Pan, Q. Liu, Z. Li, L. Liang, Q. Wu, L. K. Ang, W. Li, X. Zhao, and F. Liu, High-Performance Sliding Ferroelectric Transistor Based on Schottky Barrier Tuning, *Nano Letters* **23**, 4595 (2023).

[47] L. Li and M. Wu, Binary Compound Bilayer and Multilayer with Vertical Polarizations: Two-Dimensional

Ferroelectrics, Multiferroics, and Nanogenerators, *ACS Nano* **11**, 6382 (2017).

[48] X. Liu, Y. Yang, T. Hu, G. Zhao, C. Chen, and W. Ren, Vertical ferroelectric switching by in-plane sliding of two-dimensional bilayer WTe₂, *Nanoscale* **11**, 18575 (2019).

[49] P. Tang and G. E. Bauer, Sliding Phase Transition in Ferroelectric van der Waals Bilayers, *Physical Review Letters* **130**, 176801 (2023).

[50] S. Deng, H. Yu, J. Ji, C. Xu, and H. Xiang, Deterministic and efficient switching of sliding ferroelectrics, *Physical Review B* **111**, 174105 (2025).

[51] F. Gu, R. Jiang, and W. Gu, 2D ferroelectricity accompanying antiferro-orbital order in semi-metallic WTe₂, *arXiv:2507.18438* (2025).

[52] B. Sun, W. Zhao, T. Palomaki, Z. Fei, E. Runburg, P. Malinowski, X. Huang, J. Cenker, Y.-T. Cui, J.-H. Chu, X. Xu, S. S. Ataei, D. Varsano, M. Palummo, E. Molinari, M. Rontani, and D. H. Cobden, Evidence for equilibrium exciton condensation in monolayer WTe₂, *Nature Physics* **18**, 94 (2022).

[53] Y. Jia, P. Wang, C.-L. Chiu, Z. Song, G. Yu, B. Jäck, S. Lei, S. Klemenz, F. A. Cevallos, M. Onyszczak, N. Fishchenko, X. Liu, G. Farahi, F. Xie, Y. Xu, K. Watanabe, T. Taniguchi, B. A. Bernevig, R. J. Cava, L. M. Schoop, A. Yazdani, and S. Wu, Evidence for a monolayer excitonic insulator, *Nature Physics* **18**, 87 (2022).

[54] L. Muechler, A. Alexandradinata, T. Neupert, and R. Car, Topological Nonsymmorphic Metals from Band Inversion, *Phys. Rev. X* **6**, 041069 (2016).

[55] F. Zheng, C. Cai, S. Ge, X. Zhang, X. Liu, H. Lu, Y. Zhang, J. Qiu, T. Taniguchi, K. Watanabe, S. Jia, J. Qi, J.-H. Chen, D. Sun, and J. Feng, On the Quantum Spin Hall Gap of Monolayer 1T'-WTe₂, *Advanced Materials* **28**, 4845 (2016).

[56] H. Wang and X. Qian, Ferroelectric nonlinear anomalous Hall effect in few-layer WTe₂, *npj Computational Materials* **5**, 1 (2019).

[57] Y. Liang and L. Yang, Carrier Plasmon Induced Nonlinear Band Gap Renormalization in Two-Dimensional Semiconductors, *Phys. Rev. Lett.* **114**, 063001 (2015).

[58] D. A. Leon, C. Cardoso, T. Chiarotti, D. Varsano, E. Molinari, and A. Ferretti, Frequency dependence in *GW* made simple using a multipole approximation, *Phys. Rev. B* **104**, 115157 (2021).

[59] A. Champagne, J. B. Haber, S. Pokawanvit, D. Y. Qiu, S. Biswas, H. A. Atwater, F. H. da Jornada, and J. B. Neaton, Quasiparticle and Optical Properties of Carrier-Doped Monolayer MoTe₂ from First Principles, *Nano Letters* **23**, 4274 (2023).

[60] D. A. Leon, A. Ferretti, D. Varsano, E. Molinari, and C. Cardoso, Efficient full frequency *gw* for metals using a multipole approach for the dielectric screening, *Phys. Rev. B* **107**, 155130 (2023).

[61] A. Guandalini, D. A. Leon, P. D'Amico, C. Cardoso, A. Ferretti, M. Rontani, and D. Varsano, Efficient *GW* calculations via interpolation of the screened interaction in momentum and frequency space: The case of graphene, *Phys. Rev. B* **109**, 075120 (2024).

[62] G. Sesti, A. Guandalini, A. Ferretti, P. D'Amico, C. Cardoso, M. Rontani, and D. Varsano, Efficient *GW* calculations for metals from an accurate ab initio polarizability, *arXiv:2508.06930* (2025).

[63] N. Rytova, The screened potential of a point charge in a thin film, *Moscow University Physics Bulletin* **22**, 18 (1967).

[64] L. V. Keldysh, Coulomb interaction in thin semiconductor and semimetal films, *JETP Letters* **29**, 716 (1979).

[65] P. Cudazzo, I. V. Tokatly, and A. Rubio, Dielectric screening in two-dimensional insulators: Implications for excitonic and impurity states in graphane, *Phys. Rev. B* **84**, 085406 (2011).

[66] W. Kohn, Metals and insulators, in *Many-body physics*, edited by C. de Witt and R. Balian (Gordon and Breach, New York, 1967) pp. 351–411.

[67] L. V. Keldysh and Y. V. Kopaev, Possible instability of the semimetallic state against Coulomb interaction, *Fiz. Tverd. Tela* **6**, 2791 (1964), [Sov. Phys. Sol. State **6**, 2219 (1965)].

[68] D. Jérôme, T. M. Rice, and W. Kohn, Excitonic Insulator, *Phys. Rev.* **158**, 462 (1967).

[69] B. I. Halperin and T. M. Rice, The excitonic state at the semiconductor-semimetal transition, *Solid State Phys.* **21**, 115 (1968).

[70] J. Zittartz, Anisotropy effects in the excitonic insulator, *Phys. Rev.* **162**, 752 (1967).

[71] P. G. de Gennes, *Superconductivity of metals and alloys* (Westview Press, Boulder (Colorado), 1999).

[72] P. Giannozzi, O. Andreussi, T. Brumme, O. Bunau, M. B. Nardelli, M. Calandra, R. Car, C. Cavazzoni, D. Ceresoli, M. Cococcioni, *et al.*, Advanced capabilities for materials modelling with Quantum ESPRESSO, *Journal of physics: Condensed matter* **29**, 465901 (2017).

[73] J. P. Perdew, K. Burke, and M. Ernzerhof, Generalized Gradient Approximation Made Simple, *Phys. Rev. Lett.* **77**, 3865 (1996).

[74] D. R. Hamann, Optimized norm-conserving Vanderbilt pseudopotentials, *Phys. Rev. B* **88**, 085117 (2013).

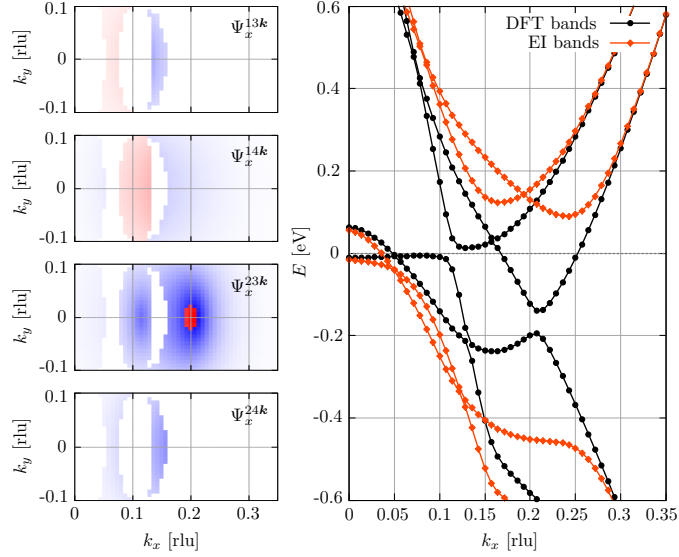
[75] H. J. Monkhorst and J. D. Pack, Special points for Brillouin-zone integrations, *Phys. Rev. B* **13**, 5188 (1976).

[76] S. Grimme, J. Antony, S. Ehrlich, and H. Krieg, A consistent and accurate ab initio parametrization of density functional dispersion correction (DFT-D) for the 94 elements H-Pu, *The Journal of Chemical Physics* **132**, 154104 (2010).

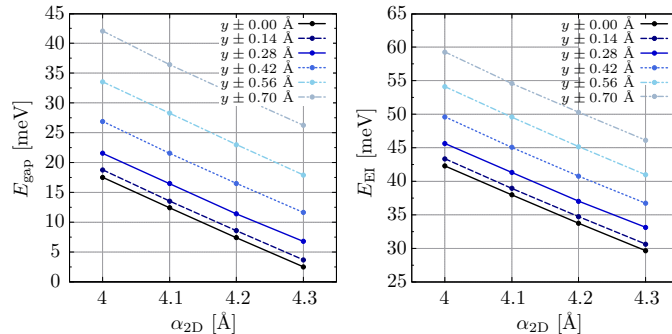
[77] S. Grimme, S. Ehrlich, and L. Goerigk, Effect of the damping function in dispersion corrected density functional theory, *Journal of Computational Chemistry* **32**, 1456 (2011).

[78] G. Henkelman, B. P. Uberuaga, and H. Jónsson, A climbing image nudged elastic band method for finding saddle points and minimum energy paths, *The Journal of chemical physics* **113**, 9901 (2000).

Supplementary Information



Supplementary Figure 1. **Model BSE and EI gap equation with four bands.** Exciton wavefunction (left) and EI bands reconstruction (right) in the four band model case. Here the exciton wave function is decomposed in the transition components $\Psi_x^{vc\mathbf{k}}$, with $v = 1, 2$ and $c = 3, 4$ the indices of the two valence and two conduction bands in ascending order of energy. The range of the color scale is $[-0.1, 0.1]$, with positive [negative] values in red [blue]. Analogously to Fig. 3 of the main text, the maximum amplitude is reached at the two locations in the Brillouin zone region that correspond to the two energy gaps along the Γ X cut between bands 2 and 3, and the corrections to the bands in the EI phase given by $\Delta_{ij}(\mathbf{k})$ (see main text) are larger where the amplitudes $\Psi_x^{vc\mathbf{k}}$ are larger. The results shown here refer to the GMS structure (black bands as in the main text). Notice that at difference with the calculations discussed in the main text, here the Brillouin zone sampling is reduced along the k_y direction: This impacts significantly the exciton binding energy, thus a lower screening parameter $\alpha_{2D} = 1.9 \text{ \AA}$ has been used to still obtain a gap > 0 in the EI phase.



Supplementary Figure 2. **Energy of the EI phase upon variation of the screening parameter.** Gap (left) and energy gain (right) in the EI phase for increasing screening of the e-h interaction. See main text for the definition of E_{EI} and α_{2D} . The connecting lines are only a guide to the eye. The plots show that although both E_{gap} and E_{EI} vary considerably with α_{2D} , the variation with respect to the top layer displacement (y as in the main text) at fixed α_{2D} is about the same for all values of α_{2D} (i.e. the lines are parallel). As a consequence, the renormalized switching barrier is the same for all these values of α_{2D} .